



Vertical height growth mechanism of hydraulic fractures in laminated shale oil reservoirs based on 3D discrete lattice modeling

Xin Chang¹ · Xingyi Wang^{1,2} · Chunhe Yang¹ · Yintong Guo¹ · Kai Wei^{1,2} · Qiang Li³ · Chengbai Jiang³

Received: 12 June 2023 / Accepted: 21 November 2023 / Published online: 8 December 2023
© The Author(s) 2023

Abstract

Bedding planes are abundant in shale oil reservoirs, but the intrinsic mechanism of fracture-height containment by these weak interfaces remains unclear. To investigate the effects of interface properties, stress conditions, and fracturing fluid viscosity on the vertical propagation of fracture heights in laminated shale oil reservoirs, a three-dimensional hydro-mechanical coupling numerical model was developed. The model is based on the 3D discrete lattice algorithm (DLA), which replaces the balls and contacts in the conventional synthetic rock mass model (SRM) with a lattice consisting of spring-connected nodes, resulting in improved computational efficiency. Additionally, the interaction between hydraulic fractures and bedding planes is automatically computed using a smooth joint model (SJM), without making any assumptions about fracture trajectories or interaction conditions. The results indicate that a higher adhesive strength of the laminated surface promotes hydraulic fracture propagation across the interface. Increasing the friction coefficient of the laminated surface from 0.15 to 0.91 resulted in a twofold increase in the fracture height. Furthermore, as the difference between vertical and horizontal principal stresses increased, the longitudinal extension distance of the fracture height significantly increased, while the activated area of the laminar surface decreased dramatically. Moreover, increasing the viscosity of the fracturing fluid led to a decrease in filtration loss along the laminar surface of the fracture and a rapid increase in net pressure, making the hydraulic fracture more likely to cross the laminar surface directly. Therefore, for heterogeneous shale oil reservoirs, a reverse-sequence fracturing technique has been proposed to enhance the length and height of the fracture. This technique involves using a high-viscosity fracturing fluid to increase the fracture height before the main construction phase, followed by a low-viscosity slickwater fracturing fluid to activate the bedding planes and promote fracture complexity. To validate the numerical modeling results, five sets of laboratory hydraulic fracturing physical simulations were conducted in Jurassic terrestrial shale. The findings revealed that as the vertical stress difference ratio increased from 0.25 to 0.6, the vertical fracture area increased by 1.98 times. Additionally, increasing both the injection displacement and the viscosity of the fracturing fluid aided in fracture height crossing of the laminar facies. These results from numerical simulation and experimental studies offer valuable insights for hydraulic fracturing design in laminated shale oil reservoirs.

Keywords Shale oil · Bedding plane · Height growth · Fluid viscosity · 3D discrete lattice method

List of Symbols

Latin Letters

a	Fracture opening, m
A_{VF}	Tension hydraulic fracture area, m ²
A_{HF}	Shear hydraulic fracture area, m ²
C	Shear strength of the macro-rock mass, Pa
d	Model size, m
E	Young's modulus, GPa
ESRA	Effective stimulated reservoir area, m ²
$F^{N\max}$	The maximum normal force of the microspring, N
$F^{S\max}$	Maximum shear force of the micro spring, N
F_i^N	Normal force component, N

✉ Xin Chang
xchang@whrsm.ac.cn

¹ State Key Laboratory of Geomechanics and Geotechnical Engineering, Institute of Rock and Soil Mechanics, Chinese Academy of Sciences, Wuhan 430071, China

² Petroleum Engineering College, Yangtze University, Wuhan 430100, China

³ Downhole Engineering Service Company, Sinopec Oilfield Service Jiangnan Corporation, Wuhan 430040, China

F_i^S	Shear force component, N
$\sum F_i$	Resultant force components acting on the node at time t , N
g	Gravity acceleration, m/s^2
G_I	Energy release rate, MN/m
h_f	Fracture height, m
\hat{H}	Dimensionless fracture height, dimensionless
I	Moment of inertia, kg m^2
k_r	Relative permeability, dimensionless
k^N	Normal stiffness, N/m
k^S	Shear stiffness, N/m
K_f	Fracture toughness, $\text{MPa m}^{1/2}$
\bar{K}_f	The apparent bulk modulus of fluid, Pa
$\sum M_i^{(t)}$	The sum of all components of the node at time t , N m
p^A	Fluid pressures at node A, Pa
p^B	Fluid pressures at node B, Pa
Δp	Increment of fluid pressure, Pa
q	Fluid flow rate, m^3/s
Q	The sum of all flow rates from all pipes connected to the node, m^3/s
r	Fracture radius, M
R	Element size, m
$R(t)$	The radius of hydraulic fracture at moment t , m
s	Saturation, dimensionless
t	Injection time, s
Δt	Time steps, s
T	The normal strength of the macro-rock mass, Pa
$u_i^{(t)}$	Displacement components of the node at time t , m
$\dot{u}_i^{(t)}$	Nodal velocity components at time t , m/s
\dot{u}_i^N	Normal velocity component, m/s
\dot{u}_i^S	Shear velocity component, m/s
ν	Poisson's ratio, dimensionless
V	Node volume, m^3
V_{inj}	The volume of the injected fluid, m^3
V_{frac}	Volume of the fracture, m^3
$W(0, t)$	Width of the fracture when the radius of the hydraulic fracture is 0, m
$W(r, t)$	Width of the fracture when the radius of the hydraulic fracture is r , m
z^A	Elevation at node A, m
z^B	Elevation at node B, m

Greek letters

α	Relaxation factor, dimensionless
α_t	Correction coefficient of the normal strength, dimensionless
α_s	Correction coefficient of the shale strength, dimensionless
β	Dimensionless coefficient, dimensionless
λ	Friction coefficient, dimensionless
μ	Fluid viscosity, mPa s

ρ	Fluid density, kg/m^3
ω_i	Angular velocity, rad/s

Introduction

Shale oil is a significant resource for increasing oil reserves and production in the future (Muther et al. 2022). However, shale oil reservoirs have very low porosity and permeability, necessitating large-scale hydraulic fracturing for economic development (Li et al. 2015; Belyadi et al. 2016; Al-Fatlawi et al. 2019; Altawati et al. 2021; WANG et al. 2021; Deng et al. 2022; Dheyauldeen et al. 2022). Additionally, these formations commonly have bedding planes (Zeng et al. 2023). For instance, in the Jurassic terrestrial shale of the Sichuan Basin in China, the density of laminar joints exceeds 50 per meter (Fig. 1). When hydraulic fractures encounter these bedding fractures, various interactions can occur, such as crossing, deflection, and termination of the fractures. Therefore, it is crucial to determine whether hydraulic fractures can overcome the constraints posed by near-wellbore bedding planes and achieve deep vertical penetration into the reservoirs. This is vital for enhancing the stimulated reservoir volume and well productivity.

Experiments have been conducted to investigate the interaction between hydraulic fractures and laminated surfaces, revealing that these weak discontinuities have a significant inhibiting effect on fracture heights. Initially, the focus was on stress contrasts and rock mechanical properties (Warpinski and Teufel 1987; Beugelsdijk et al. 2000; Li et al. 2018; Tan et al. 2020; Heng et al. 2020). However, in recent years, more attention has been given to the inherent properties of the bedding planes and the approach angle. Guo et al. (2021) suggested that a complex fracture network can form when the bedding dip angle is less than 30° and the vertical in situ stress difference is 10 MPa. Similarly, Zhou et al. (2022) found that the bedding dip angle is not the sole factor influencing fracture propagation; the micromechanical properties of adjacent beds also play a significant role. Zhang et al. (2023b) observed that when hydraulic fractures encountered low-brittleness sandstone interbeds, plastic deformation occurred within the interbeds, reducing the ability of the fractures to penetrate the interface and interbeds. Liu et al. (2022a) discovered that complex fracture networks are more likely to form when the maximum principal stress direction is perpendicular to the bedding plane. Furthermore, the fracture initiation pressure gradually decreases as the bedding dip angle increases. However, due to sample size limitations, physical simulation experiments only allow for qualitative analysis of the effects of bedding planes on vertical fracture propagation under different parameters, and real-time monitoring of the failure process is not feasible. Additionally, laboratory experiments typically utilize large cubic outcrop

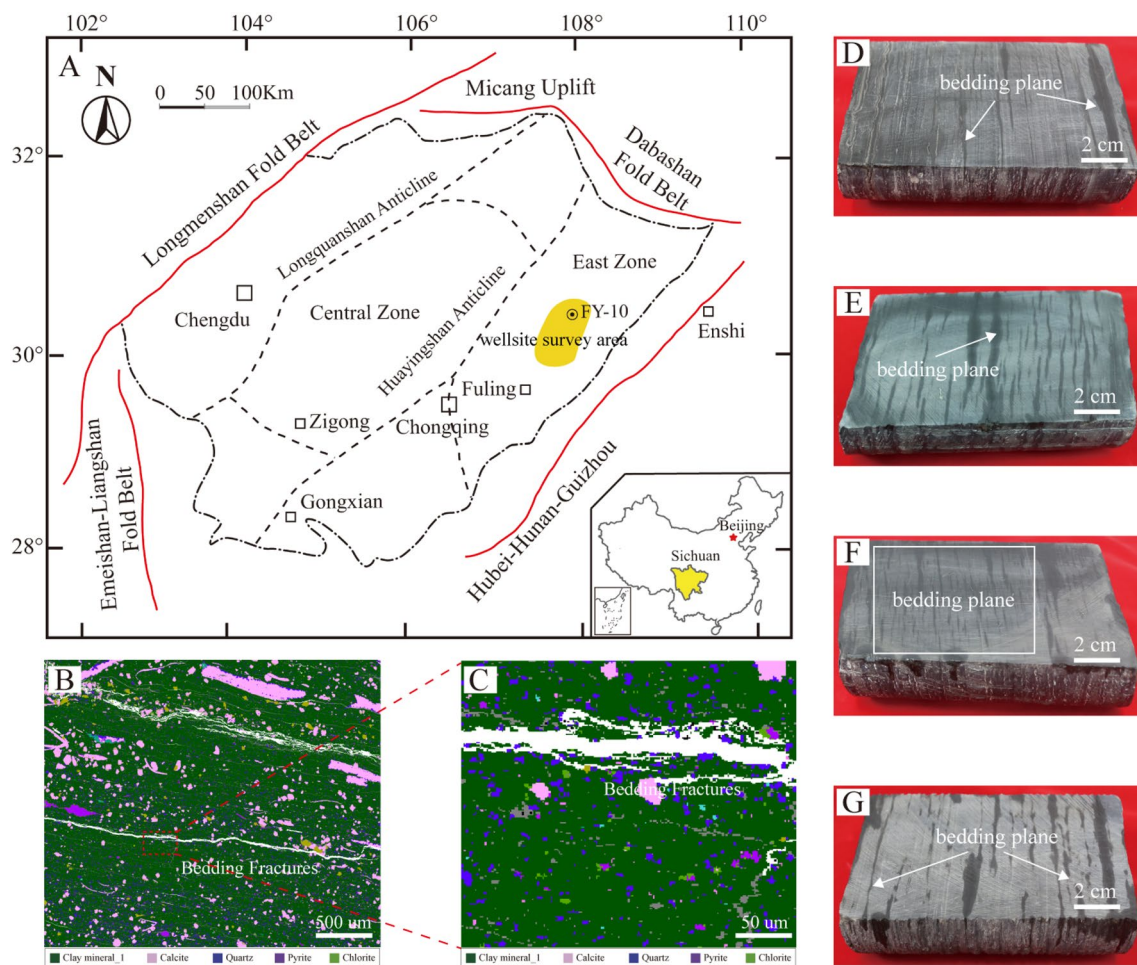


Fig. 1 Laminae characteristics of terrestrial shales from the Dong Yuemiao Formation in the Fuxing Sag, Sichuan Basin, China. **A** Sketch map showing the location of the Fuxing Sag; **B** and **C** QEM-

SCAN image of laminated shale sample from XY-3 well; **D** through **G** Core images of laminated shale, XY-3 well

samples or artificial samples with pre-existing discontinuities, making it challenging to control the mechanical properties of the laminated surfaces and quantitatively study the effects of various factors on the expansion pattern of seam height.

Moreover, accurately determining the anisotropic mechanical properties of shale is crucial for studying the initiation and propagation of hydraulic fractures in terrestrial shale. Determining these properties using conventional methods is time-consuming and may even become impractical. During the recovery process, large shale samples frequently experience fragmentation due to their inadequate mechanical stability. There has been an ongoing discussion regarding this issue, which has prompted the development of new techniques for characterizing them using small samples such as cutting and chips. One interesting method is based on nanoindentation or two-scale finite element methods. Li and Sakhaee-Pour (2016) proposed a conceptual model to consider the effective stiffness of the solid grain, which

is determined by the nanoindentation, and scaled up these results to the core scale. Further, they proposed a two-scale model to predict the elastic modulus of shale at the core scale. This model considers the complex geometry of voids and solid particles (Sakhaee-Pour and Li 2018; Esatyana et al. 2020). Esatyana et al. (2021) conducted a quantitative characterization of shale anisotropic fracture toughness at a sub-centimeter scale using nanoindentation. Alipour et al. (2021) then introduced machine learning to nanoindentation experiments to further improve the accuracy of the shale fracture toughness test results. However, numerical simulations offer a viable approach to investigate the expansion behavior of hydraulic fractures as they approach laminar surfaces with varying properties.

Many numerical methods have been employed to study the interaction of hydraulic fractures with bedding planes, such as the finite element method (Wang et al. 2015; Chang et al. 2017), the extended finite method (Zeng et al. 2018; Tan et al. 2021), the boundary element method (Gu et al.

2008, 2012; Tang et al. 2019; Xie et al. 2020), the discrete element method (Yushi et al. 2016; Huang et al. 2022), the combined finite-discrete element method (Zhao et al. 2014; Wu et al. 2022), the phase field method (Qin and Yang 2023), and the peridynamics method (Qin and Yang 2023). In these models, anisotropic or transverse isotropic ontological constitutive equations have been commonly used to characterize the heterogeneity caused by bedding planes. However, there is still a lack of understanding regarding the propagation mechanism of hydraulic fractures in heterogeneous reservoirs and the intrinsic mechanism of their interaction with bedding planes. For example, in the boundary element method, a predetermined criterion is required to determine whether the hydraulic fracture crosses the bedding plane. In addition, although the hybrid use of finite element and cohesion zone models can accurately calculate the stress and displacement fields around the crack, it necessitates local mesh refinement near the bedding plane, and the crack propagation pattern is closely linked to the mesh size. Furthermore, most studies have been limited to two-dimensional problems, making it challenging to analyze the opening morphology and area of the bedding plane. These limitations can be overcome by employing a three-dimensional discrete lattice model (Xsite) to separately describe the matrix and the bedding plane (Damjanac and Cundall 2016a). The lattice model allows fracture through the breakage of springs along with slip along pre-existing joints using a smooth joint model logic (Pierce et al. 2007). It can represent both movement on pre-existing joints (sliding and opening) and fracture of intact rock. The code accounts for the interaction between hydraulic fractures as well as between fractures and pre-existing joints. Interactions are resolved automatically, using basic principles of mechanics, without any assumptions about the fractures' trajectories or conditions of interaction.

Frankly, the propagation pattern of hydraulic fractures is typically affected by stress conditions (magnitude, direction, and difference), rock properties (Young's modulus, Poisson's ratio, and fracture toughness), and structural properties (such as laminations and natural fractures). However, these parameters are inherent to reservoirs and cannot be artificially changed. In recent studies, some scholars have proposed that the expansion of hydraulic fractures through layers can be achieved by selecting the optimal fluid viscosity and injection rate (Rueda Cordero et al. 2019; Zhao et al. 2020). Nevertheless, the exact mechanism by which these two parameters influence the ability of hydraulic fractures to penetrate remains unclear.

In this study, a 3D hydro-mechanical coupling numerical model was established to investigate the propagation of hydraulic fractures in a homogeneous shale oil reservoir. The model analyzes the behavior of hydraulic fracture propagation considering various geological and engineering

parameters, such as the cohesive strength of the bedding planes, the difference between vertical stress and minimum horizontal principal stress, and the viscosity of the fracturing fluid. Moreover, an innovative reverse-sequence fracturing technique is proposed and validated through indoor hydraulic physical simulation experiments to enhance the fracture length and height in shale oil reservoirs. The findings of this research provide valuable insights for optimizing the design of hydraulic fracturing in shale oil reservoirs.

Modeling and methods

The 3D HF simulation software XSite, developed by Itsaca Corporation, was utilized in this study (Damjanac and Cundall 2016a). This software is based on a 3D discrete lattice method and can effectively simulate the propagation of multiple HFs in naturally fractured reservoirs, including laminar shale oil reservoirs and pre-salt carbonate reservoirs (Soltanmohammadi et al. 2021).

The 3D discrete lattice method involves a reduced cohesive particle model based on discrete lattice theory, which can be used to simulate the deformation and fracture of rocks, fabricated via synthetic rock mass (SRM) techniques (Wang et al. 2020; Bakhshi et al. 2021). As depicted in Fig. 2, The synthetic rock mass (SRM) concept is a fractured rock mass idealization in which the intact matrix is represented by the particle-based model and the pre-existing joints by the smooth joint model (SJM). The original implementations of the SRM models have used the general-purpose codes PFC2D and PFC3D, which employ assemblies of circular/spherical particles bonded together. However, the lattice is an array of 3D particles connected through breakable nonlinear springs. The mechanical properties of the springs represent the macroscopic strength of the rock mass. The lattice ruptures when the tensile strength of the spring exceeds a threshold. Fluid flow within the fracture (including joints) and matrix is carried out in a series of pipes that are connected to the center of the springs. An arbitrary discrete fracture network model can be embedded into the model. To define the pre-existing joints in the rock mass, a smooth joint model is utilized, which can precisely represent the opening, slip, and closure of the joint surface. It overcomes all main limitations of the conventional methods for the simulation of hydraulic fracturing in jointed rock masses and is computationally more efficient than PFC-based implementations of the SRM method (Potyondy and Cundall 2004; Potyondy 2015).

Mechanical model

Explicit numerical methods are used in the 3D discrete lattice approach to directly calculate the complex behavior of

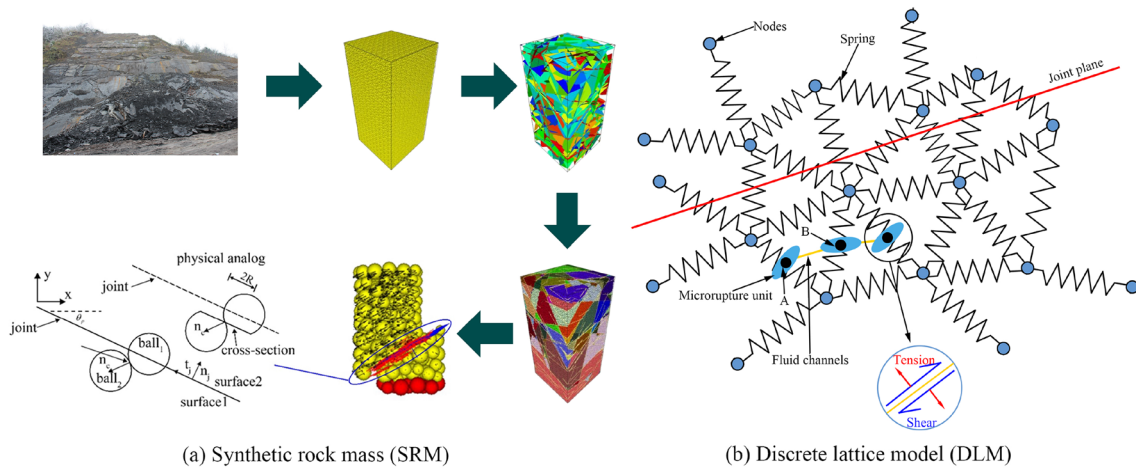


Fig. 2 Schematic of the 3D discrete lattice method (Zhang et al. 2023a)

fracture, slip, opening, and closure of the joints. The translational degrees of freedom for each lattice point can be obtained from the following equation (Damjanac and Cundall 2016b):

$$\begin{aligned} \dot{u}_i^{(t+\Delta t/2)} &= \dot{u}_i^{(t-\Delta t/2)} + \sum F_i^{(t)} \Delta t / m \\ \dot{u}_i^{(t+\Delta t)} &= \dot{u}_i^{(t)} + \dot{u}_i^{(t+\Delta t/2)} \Delta t \end{aligned} \tag{1}$$

The angular velocity component of the lattice point at moment t can be derived from the following equation:

$$\omega_i^{(t+\Delta t/2)} = \omega_i^{(t-\Delta t/2)} + \frac{\sum M_i^{(t)}}{I} \Delta t \tag{2}$$

Equations (3) and (4) characterize the correspondence between the micromechanical properties of the spring and the rock mass macroscopic strength:

$$F^{N \max} = \alpha_t TR^2 \tag{3}$$

$$F^{S \max} = \lambda F^{N \max} + \alpha_s CR^2 \tag{4}$$

where α_t and α_s denote tensile and shear strength calibration factors, respectively.

The tangential and normal stresses of the spring can be obtained from the relative displacement of the nodes.

$$\begin{aligned} F_i^N &\leftarrow F_i^N + i^N k^N \Delta t \\ F_i^S &\leftarrow F_i^S + i^S k^S \Delta t \end{aligned} \tag{5}$$

When their strength (in tension or shear) is surpassed, the springs will be broken. After spring damage, microcracks form and the spring stress returns to zero.

Pre-existing joints in shale can significantly affect the extensional pattern of HF, fracture extension pressure, and the filtration rate of fracturing fluid. In situ stresses

and pore pressures are altered by the formation of HF, resulting in sliding and microseismic activity in the joints surrounding the HF. Furthermore, the rupture of joints obeys the smooth joint model and is not affected by the surface roughness.

The spring normal force is positive in tension and negative in compression. The normal force obtained from Eq. (5) can be used to determine whether a spring has broken: thus, if $F_i^N > F^{N \max}$, then $F_i^N = 0$, $F_i^S = 0$, spring rupture occurs. Note that for a spring (describe a joint), the shear stress component should be less than the maximum frictional resistance.

$$\text{If } |F_i^S| > \lambda |F_i^N| \text{ then } F_i^S \leftarrow F_i^S \frac{\lambda |F_i^N|}{|F_i^S|} \tag{6}$$

In this model, the HF propagates along the direction of the maximum energy release rate. The criterion for fracture initiation is that G_I reaches the critical G_{IC} :

$$G_I = \frac{K_I^2}{E(1-\nu^2)} \tag{7}$$

where G_I is the energy release rate, K_I is the fracture toughness, E is the Young's modulus, and ν is the Poisson's ratio

Fluid flow in the fracture

The fracturing fluid flows in a series of connected pipes. These pipes are located in the center of a broken spring or a spring representing a pre-existing joint (i.e., a spring that intersects the surface of a pre-existing joint). In this model, the fracturing fluid flow in the pipe obeys the planar Poiseuille equation:

$$q = \beta k_r \frac{a^3}{12\mu} [p^A - p^B + \rho g(z^A - z^B)] \quad (8)$$

where k_r is closely related to the saturation s of the fluid elements:

$$k_r = s^2(3 - 2s) \quad (9)$$

Additionally, the pressure increment over the flow time step can be calculated as follows:

$$\Delta p = \frac{Q}{V} \bar{K}_f \Delta t \quad (10)$$

where Q is the sum of the fracture volume flows from all the pipes connected to the node.

When the fracture width is large or the fracturing fluid viscosity is small, the calculation becomes extremely inefficient using the explicit iteration algorithm. Then, a relaxation scheme is an excellent solution to this problem. In this scheme, the fluid pressure is adjusted at each flow time step to make the fracture volume match the injected fluid volume. The pressure correction value in one iterative can be calculated by the following equation:

$$\Delta p^{<i>} = \alpha \frac{V_{inj} - V_{frac}}{V_{frac}} \quad (11)$$

where V_{inj} and V_{frac} are the volume of the injected fluid and the fracture, respectively.

Fluid–solid coupling

Fluid flow and mechanical deformation are fully coupled in the 3D discrete lattice approach. Fluid flow in stress-induced fractures or pre-existing natural fractures is influenced by permeability. The permeability of the crack is determined by the opening and subsequent strain of the rock model. Fluid pressure acts on the crack surface and impacts the mechanical properties of the rock. Rock deformation causes

variations in fluid pressure and fracture width, which in turn affects fracture permeability.

Model validation

In this study, the simulation results from the 3D lattice code were compared with the analytical solution of the penny-shaped fracture model (Fig. 3) for zero fracture toughness and no leak-off case provided by Peirce and Detournay (2008).

In this case, only viscous dissipation takes place and all the injected fluid is contained in the fracture. The non-steady response of rock is viscosity-dominated, which corresponds to the M-asymptote. The variation of the fracture radius R and aperture W at different injection moments can be obtained from the following equation:

$$R(t) = 0.6944 \left(\frac{E' Q^3 t^4}{\mu'} \right)^{1/9} \quad (12)$$

$$W(0, t) = 1.1901 \left(\frac{\mu'^2 Q^3 t}{E'^2} \right)^{1/9} \quad (13)$$

$$W(r, t) = 1.1901 \left(\frac{\mu'^2 Q^3 t}{E'^2} \right)^{1/9} (1+r)^{0.487} (1-r)^{2/3} \quad (14)$$

where t denotes the injection time, and x is the coordinate in the axis system with the injection point as the reference. The three scalars r , E' and μ' defined as:

$$r = x/R(t), \quad \mu' = 12\mu, \quad E' = E/(1 - \nu^2) \quad (15)$$

The parameter values listed in Table 1 were used in the following calculations. In addition, the tensile strength of the rock is zero, and the in situ stresses are also zero. Figure 4a provides the HF expansion morphology at 10 s of elapsed time. The aperture profiles at three different injection moments are shown in Fig. 4b together with the asymptotic

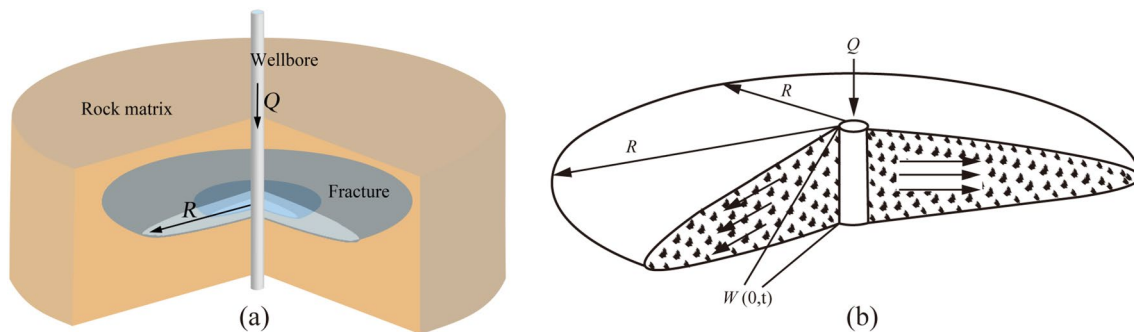


Fig. 3 Schematic diagram of the Penny-type crack

Table 1 Properties used in model validation

Young's modulus E	Poisson's ratio ν	Fracture toughness K_{IC}	Injection rate Q	Dynamic viscosity μ
70.0 GPa	0.22	0.001 MPa m ^{0.5}	0.01 m ³ /s	0.001 Pa s

solutions given by Savitski and Detournay (2002). Notably, despite that there is scatter, the numerical results and the analytical solutions are well aligned.

Furthermore, the ability to accurately simulate HF growth in the presence of stress gradients or sudden stress changes is a fundamental requirement of the numerical model. Wu et al. (2008) conducted a polymethyl methacrylate block test to investigate the HF crossing a sudden stress jump and penetrating a lower stress zone. The PMMA block geometry and stress profile are illustrated in Fig. 5.

A comparison of the numerical and experimental results of this test was made. The numerical model's geometry and boundary conditions are in line with the experiment, and the parameters used can be found in the literature. The thickness of the pay zone is 50 mm, and the upper side of the zone is a high-stress blocking layer, in which the stress is 4.2 MPa higher, while the lower side is a low-stress zone, in which the stress is reduced by 2 MPa. As illustrated in Fig. 6, the numerical results are extremely similar to the experimental results. Although the injection point is located near the high-stress layer, the seam height is challenging to extend upward and primarily occurs in the low-stress zone. This is primarily due to the lower minimum horizontal stress in the rock, which results in a relatively high net pressure within

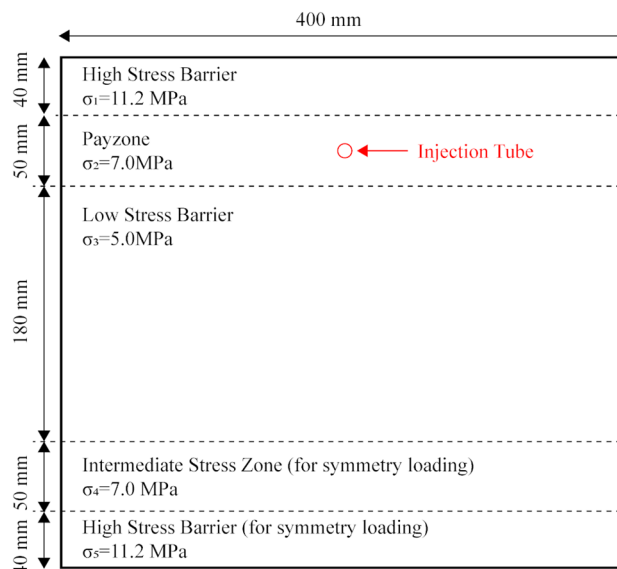


Fig. 5 The model geometry and stress loading conditions

the fracture and a significant stress intensity factor at the fracture tip (Chang et al. 2022).

Notably, the simulation results of the numerical model are very similar to both the analytical solution and the experimental results, indicating that our 3D hydraulic fracturing model is accurate. One limitation in modeling is that the runtime of the model is highly dependent on the resolution, particularly when a uniform resolution is applied. Roughly, the simulation time is inversely proportional to the resolution power of five. This sensitivity can be reduced

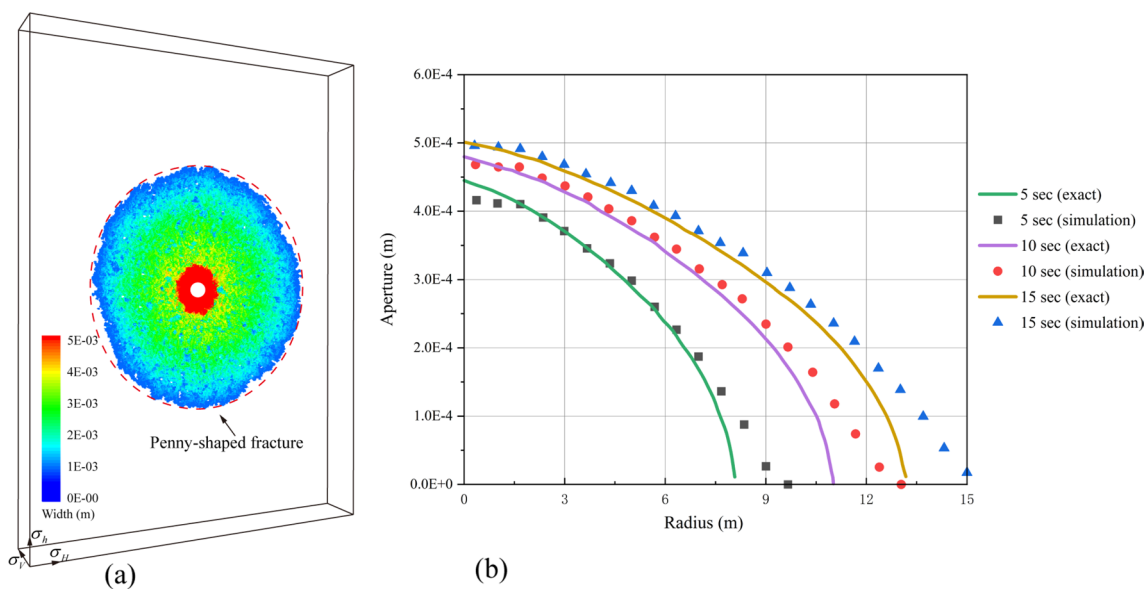


Fig. 4 Aperture profiles for three different moments under zero fracture toughness conditions

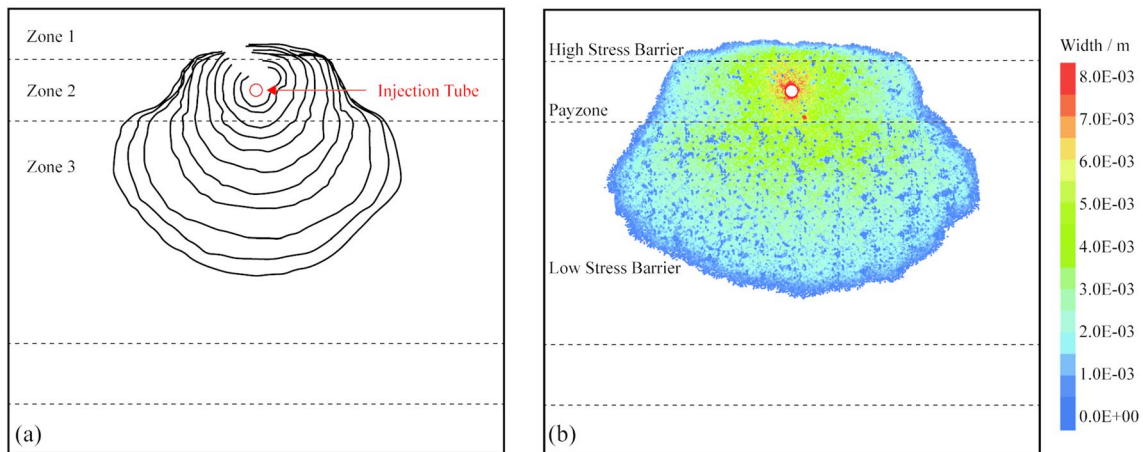


Fig. 6 Comparison of experimental results with numerical results

if variable resolution (i.e., finer around the injection clusters and coarser close to the far-field boundaries) is used.

Analysis of factors affecting fracture propagation

The numerical model is shown in Fig. 7, with the horizontal wellbore running through the center of the sample. The rock model size is $20\text{ m} \times 20\text{ m} \times 20\text{ m}$. To increase the calculation efficiency, the model is preset with four bedding planes. The planes are symmetrically distributed concerning the wellbore, and they are 5 m apart from each other. The horizontal wellbore is parallel to the direction of the minimum in situ stress. The model parameters are presented in Table 2. Using this model, the longitudinal propagation pattern of fractures in laminated shale oil reservoirs under the influence of multiple parameters can be studied.

To quantitatively characterize the performance of reservoir stimulation under the impacts of different parameters, the dimensionless fracture height \hat{H} and the effective stimulated reservoir area (ESRA) are proposed:

$$\hat{H} = \frac{h_f}{d} \quad (16)$$

$$ESRA = A_{VF} + A_{HF} \quad (17)$$

where d is the model size, m; $ESRA$ is the effective reservoir modification area, m^2 ; A_{VF} is the vertical HF area, m^2 ; and A_{HF} is the horizontal laminar fracture area, m^2 .

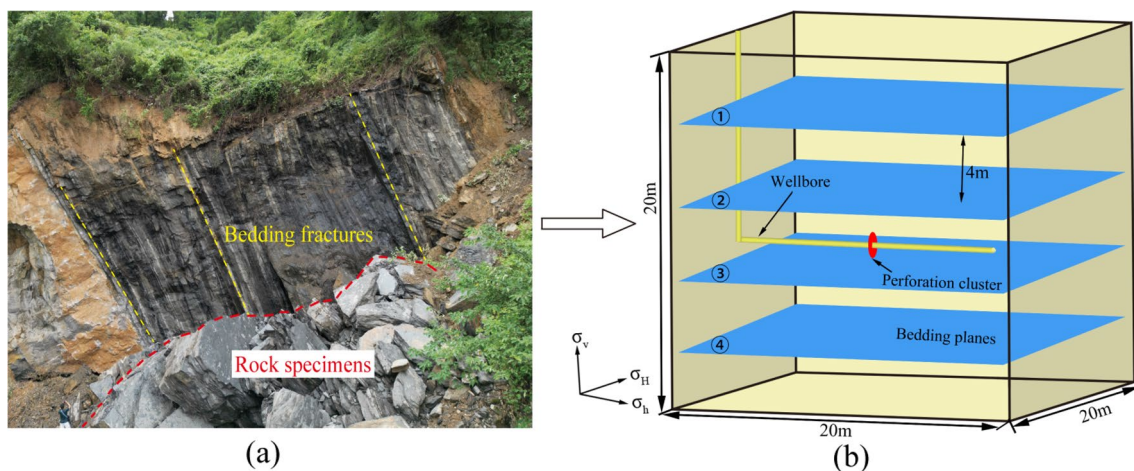


Fig. 7 Sketch of the numerical model. The borehole is shown in yellow, cluster in red

Table 2 Rock and fluid properties for the parametric analyses

Material properties	Value	Units
<i>Rock matrix</i>		
Young's modulus E	15	GPa
Poisson's ratio ν	0.35	–
Rock density ρ_m	2600	Kg/m ³
Tensile strength T_m	4	MPa
Fracture toughness K_{IC}	0.5	MPa m ^{0.5}
Permeability k_m	1E-18	m ²
Porosity φ_m	0.01	–
<i>In situ stresses</i>		
Vertical stress σ_v	20	MPa
Maximum horizontal principal stress σ_H	15	MPa
Minimum horizontal principal stress σ_h	10	MPa
<i>Laminated plane</i>		
Cohesion c_0	2	MPa
The angle of internal friction θ	25	
Initial aperture b_0	0.1	mm
Initial normal stiffness k_n	30	GPa/m
Shear stiffness k_s	15	GPa/m
Tensile strength T_J	0.5	MPa
<i>Fluid</i>		
Fluid density ρ_L	1000	Kg/m ³
Injection rate Q	3	m ³ /min
Fluid viscosity μ	10	mPa s

Effects of cementation strength of bedding planes

Heng et al. (2020) and Li et al. (2022) experimentally investigated the cementation properties of bedding planes of shale. It was discovered that the friction coefficient of shale bedding planes is between 0.37 and 0.75. In this section, three different strength levels of the bedding planes (friction coefficient = 0.15, 0.49, and 0.91, respectively) are considered.

As shown in Fig. 8, when the cementation strength of the bedding planes is 0.15, as the HF reaches the planes, the fracturing fluid is rapidly filtered out along the bedding planes, and the fracture height stops increasing. As the cementation strength increases, the inhibitory effect of the bedding planes on the fracture height is weakened. When the friction coefficient of the bedding planes is 0.49, the HF breaks through the two adjacent planes and extends to the external bedding planes. When the friction coefficient increases to 0.91, the HF successively crosses the four planes, and the fracture height reaches the maximum longitudinal propagation distance. The fracture becomes approximately circular.

As shown in Fig. 9, when the friction coefficient of the bedding plane increases from 0.15 to 0.91, the dimensionless fracture height increases from 0.2 to 0.75, and the fracture

height increases almost two times. The effective stimulated reservoir area is 540 m², 350 m², and 270 m² for the three different levels of bedding plane cementation strength. Although the post-fracturing ESRA is the largest for weakly cemented reservoirs, the horizontal bedding-plane area accounts for as much as 87.28%. Since the horizontal fracture opening is usually small, the proppant is difficult to enter, so its contribution to production is very limited.

Effects of vertical in situ stress difference

This section examines the impact of vertical in situ stress difference on the longitudinal propagation of fractures. The vertical stress difference is the disparity between the vertical stress and the horizontal minimum in situ stress. The model assumes that the maximum horizontal principal stress is 15 MPa, the minimum horizontal principal stress is 10 MPa, and the vertical in situ stresses are 10, 15, and 20 MPa, respectively. The simulation results are depicted in Fig. 10.

When the vertical in situ stress difference is 0 MPa, the normal stress acting on the bedding plane is low making the plane more prone to debonding slip. As the fracturing fluid is continuously injected, the HFs are stopped by the adjacent planes. Subsequently, the directions of the fractures change, and a significant amount of fracturing fluid is lost into the bedding planes. At the end of injection, a rectangular fracture surface is formed inside the sample, and the fracture height is the distance between the two adjacent bedding planes. The ESRA value is 480 m² because a large area of the bedding plane is activated (Fig. 11).

As the vertical in situ stress difference increases, it becomes more difficult for the bedding planes to open, and the inhibitory effect on the fracture height is significantly reduced. When the vertical in situ stress difference is 5 and 10 MPa, the dimensionless fracture height is 0.6 and 0.9, respectively. In addition, when the vertical in situ stress difference increases from 0 to 10 MPa, the ESRA decreases from 480 m² to 320 m², while the fracture complexity decreases significantly. Therefore, when fracturing is performed in reservoirs with large vertical in situ stress differences, despite the considerable longitudinal penetration distance of HFs, the horizontal spread of the cracks is limited, resulting in a smaller ESRA.

Effects of fracturing fluid viscosity

It has been observed that increasing both the fracturing fluid discharge rate and viscosity can promote the longitudinal propagation of fractures and increase the net pressure of the fluid in fractures (Yushi et al. 2017). Due to the narrow interval of injection rate variation in the field, we only examine the impact of fracturing fluid viscosity on the propagation

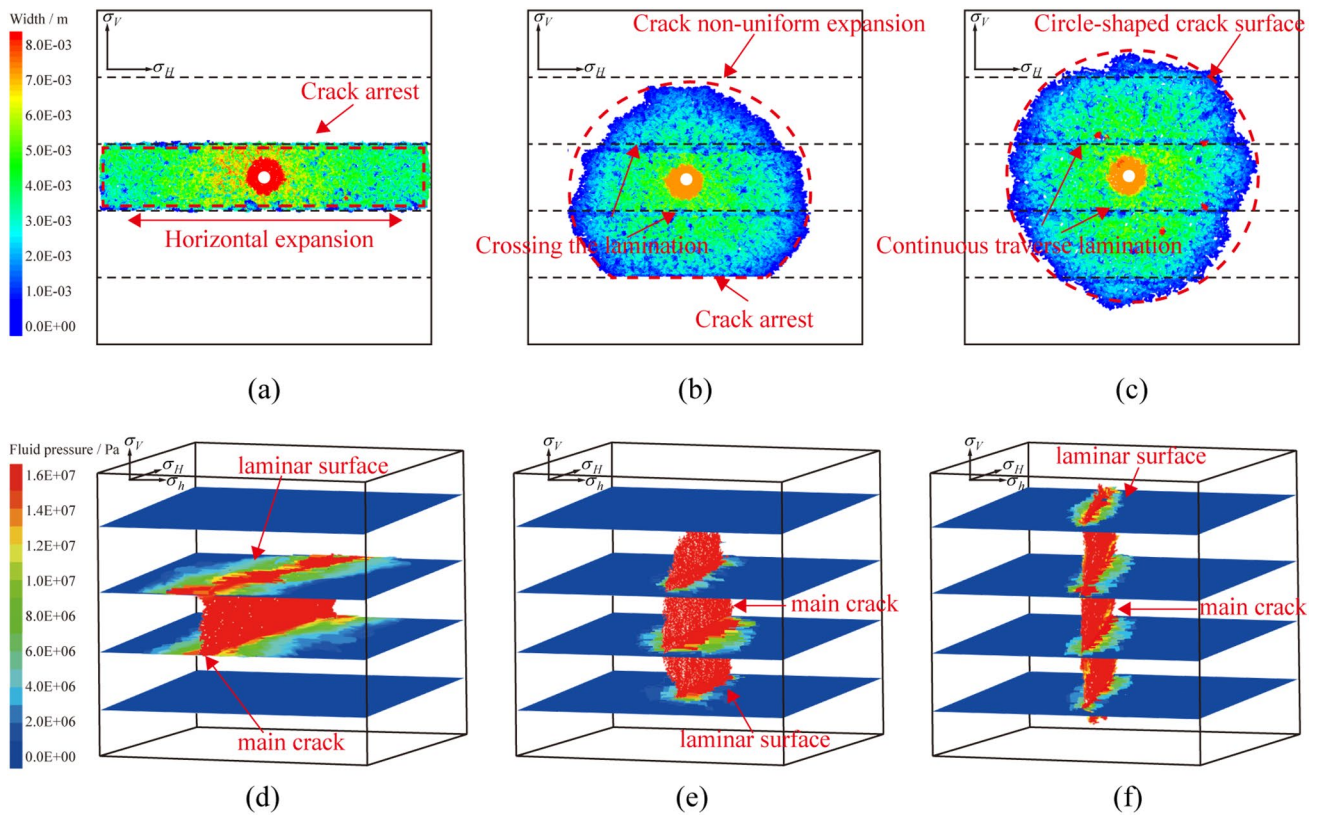


Fig. 8 Cloud map of crack width and pressure distribution under different bedding planes' cementation strength

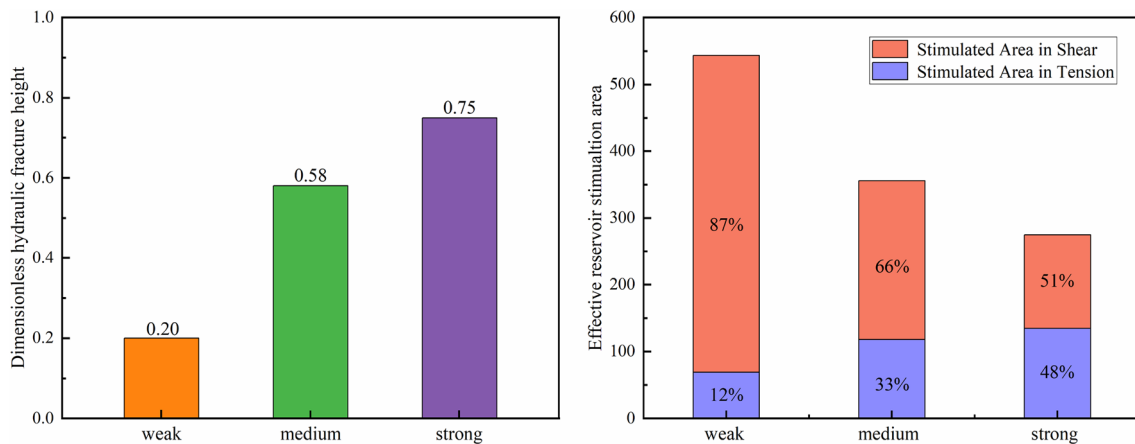


Fig. 9 Variations of fracture height and effective fracture area with cementation strength of the bedding plane

pattern of hydraulic fractures in this section. The study sets the fracturing fluid viscosity at 5 and 200 mPa s and keeps the injection rate constant at 0.05 m³/s. The fracturing fluid injection volume remains constant at 0.5 m³ for all cases.

As shown in Fig. 12, when the fracturing fluid viscosity is low (5 mPa s), the HF's are more easily terminated by the bedding planes; thus, the fracture height stops increasing, and a large amount of fracturing fluid is lost into the bedding

fractures. Hence, for finely laminated shale reservoirs, the use of low-viscosity fracturing fluid can effectively increase the fracture complexity near the wellbore, but the fracture height is limited. Meanwhile, owing to the small aperture of the bedding fractures, it is difficult for the proppant to enter them. At later stages, under pressure from the overlying rock, these bedding fractures will close again, which significantly affects the long-term conductivity of the fracture

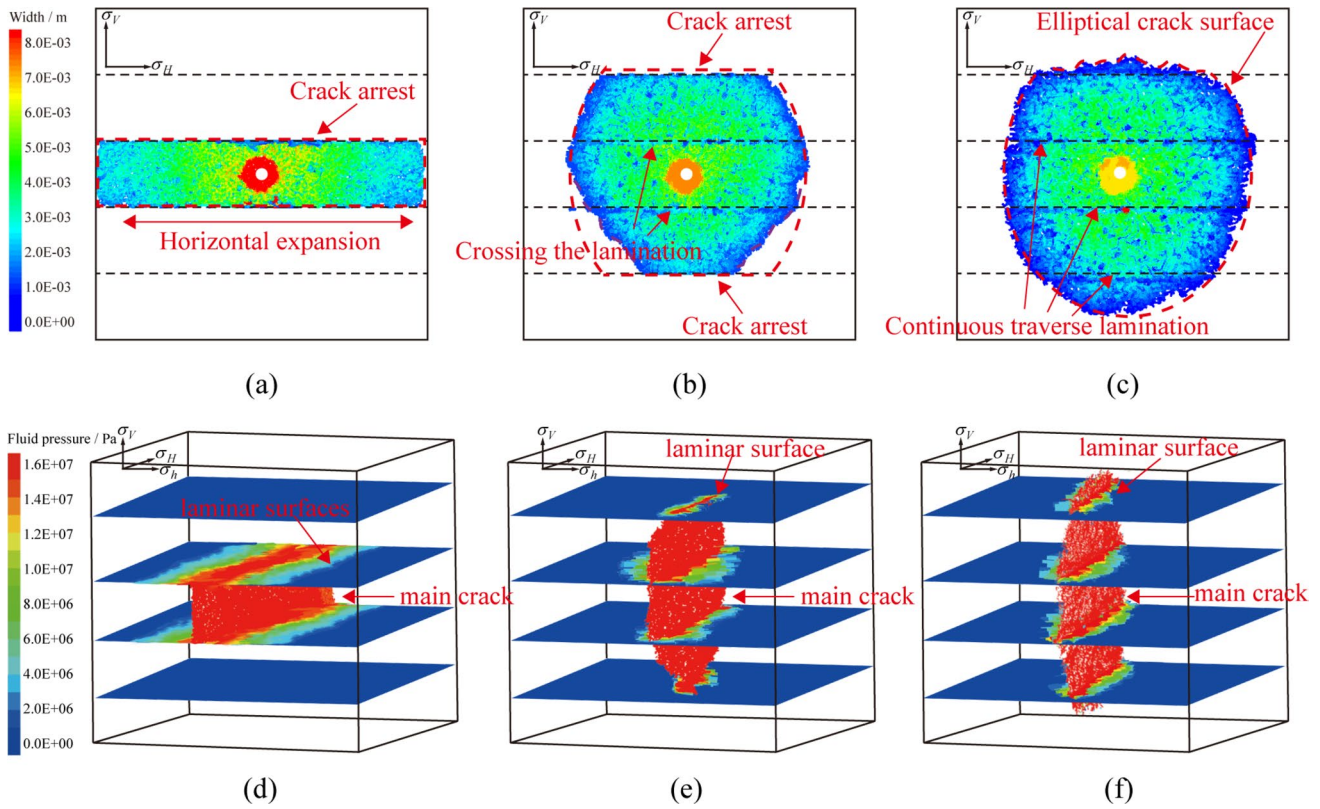


Fig. 10 Cloud map of main crack width and pressure distribution under different vertical in situ stress difference

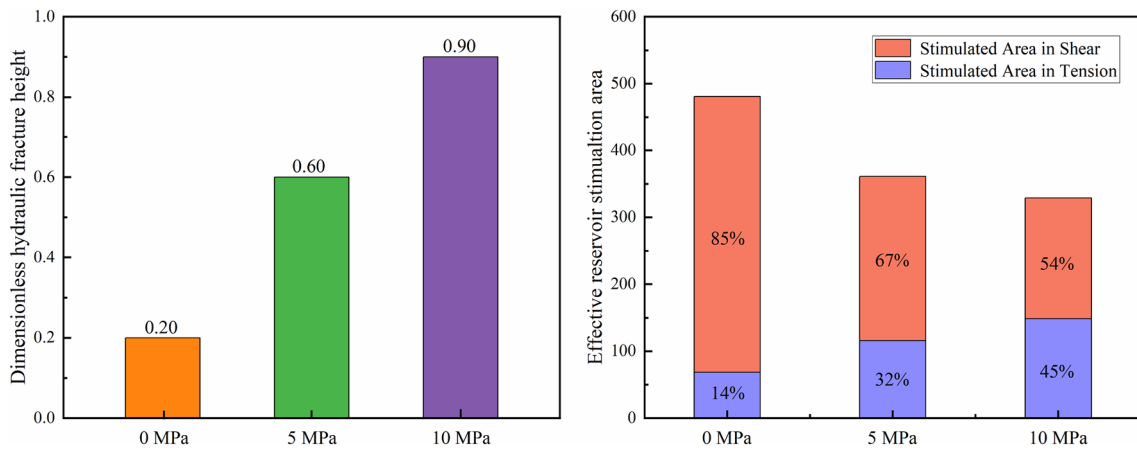


Fig. 11 Variations of dimensionless fracture height and effective fracture area with vertical in situ stress difference

network. With the increase of fracturing fluid viscosity, the restricting effect of the laminar surface on the fracture height gradually decreases. When the fracturing fluid viscosity is 200 mPa s, HF's successively cross two adjacent bedding planes, and the fracture propagation rates in the vertical and lateral directions are almost equal. However, owing to the higher viscosity, the flow resistance of the fracturing fluid in the bedding plane increases, resulting in a significant

reduction in the activated area of the bedding plane and a lower overall fracture network complexity.

The effects of alternating injection of high- and low-viscosity fracturing fluids on the fracture morphology are also investigated to maximize the degree of activation of laminated shale oil reservoirs. Highly viscous fracturing fluid of 200 mPa s is injected at 0–5 s, and low-viscosity fracturing fluid of 5 mPa s is injected at 5–10 s. The other

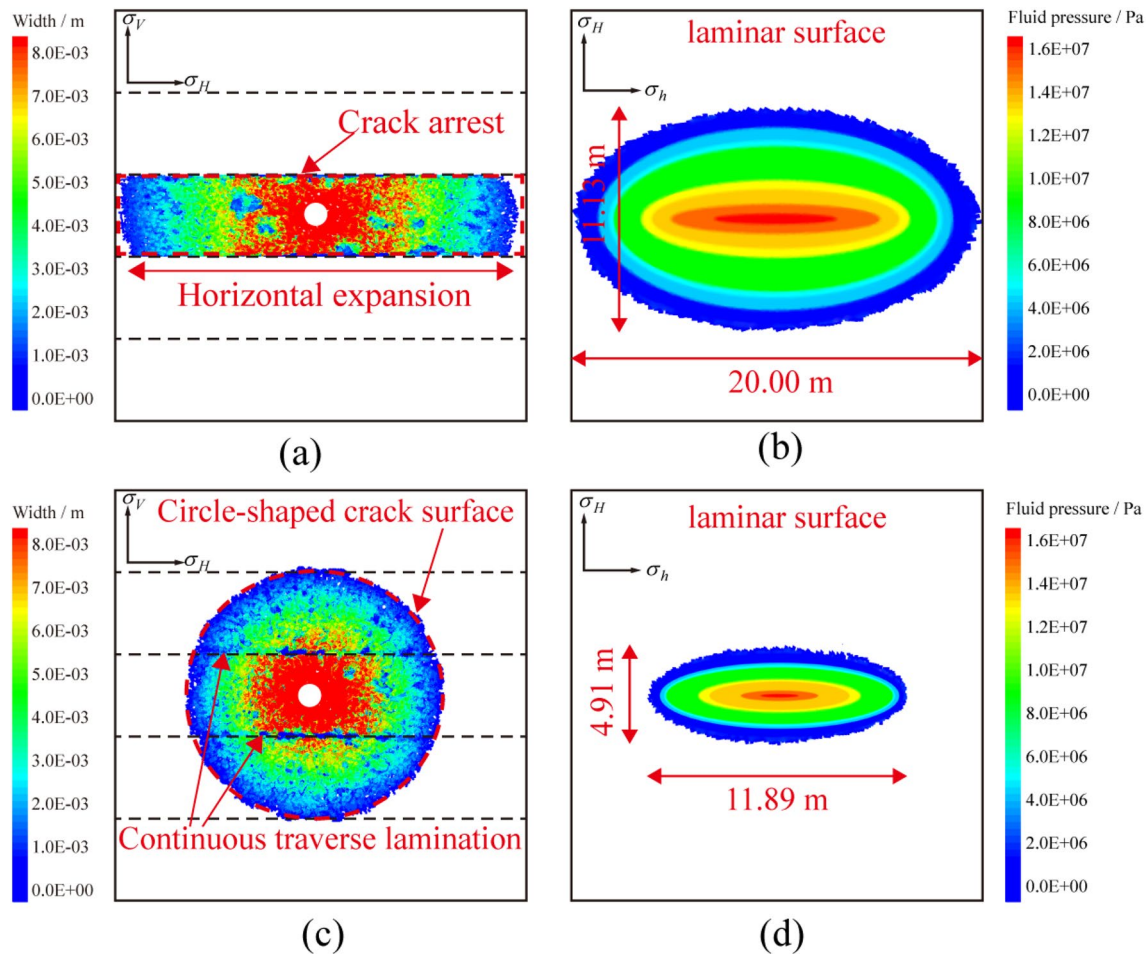


Fig. 12 Longitudinal and horizontal crack extension patterns under different fracturing fluid viscosities (**a, b**: 5 mPa s; **c, d**: 200 mPa s)

input parameters and stress boundary conditions are consistent with the above model.

For shale oil reservoirs with well-developed laminations, if low-viscosity slickwater fracturing fluid is used throughout the process, the hydraulic fracture propagation is easy to capture directly by the adjacent bedding planes. This results in a large quantity of fluid being retained around the wellbore, which significantly restricts hydraulic fracture propagation to the deeper part of the formation and greatly affects the volume of reservoir modification. Therefore, a reverse-sequence fracturing technique was proposed, which initially uses high-viscosity fracturing fluid to form a long-distance effective main fracture to break through the near-well laminations and then uses low-viscosity fracturing fluid to activate the laminations interacting with the main fracture at a later stage to form a kind of fishbone-shaped complex fracture network. This approach aims to maximize the complexity of the fracturing fractures and the stimulation effect.

As illustrated in Fig. 13, during the early high-viscosity fracturing fluid injection stage, HFs successively penetrate through the two adjacent bedding planes and approach the

top and bottom planes. Owing to the high viscosity of the fracturing fluid, the seepage resistance is high; thus, only a little fracturing fluid filter loss is observed on the planes. In the later stage of low-viscosity fracturing fluid injection, HFs continue to propagate upward and penetrate through the top and bottom bedding planes. In addition, a large amount of low-viscosity fracturing fluid is lost into the bedding fractures, and the horizontal extent of the fractures increases significantly. Finally, a fishbone-shaped complex fracture network characterized by predominant longitudinal HFs and multiple minor bedding fractures is formed. This effectively enhances the laminated reservoir stimulation effects of hydraulic fracturing.

Figure 14 shows the variations of the main and bedding fracture areas with time during fracturing. When highly viscous fracturing fluid is injected at 0–5 s, the growth rate of the main fractures is 12.32 m²/s, and that of the bedding fractures is 8.89 m²/s. The vertical propagation capacity of the HFs is much higher than the opening capacity of the bedding planes. At 5–10 s, when low-viscosity fracturing fluid is injected, the growth rate of the main fracture

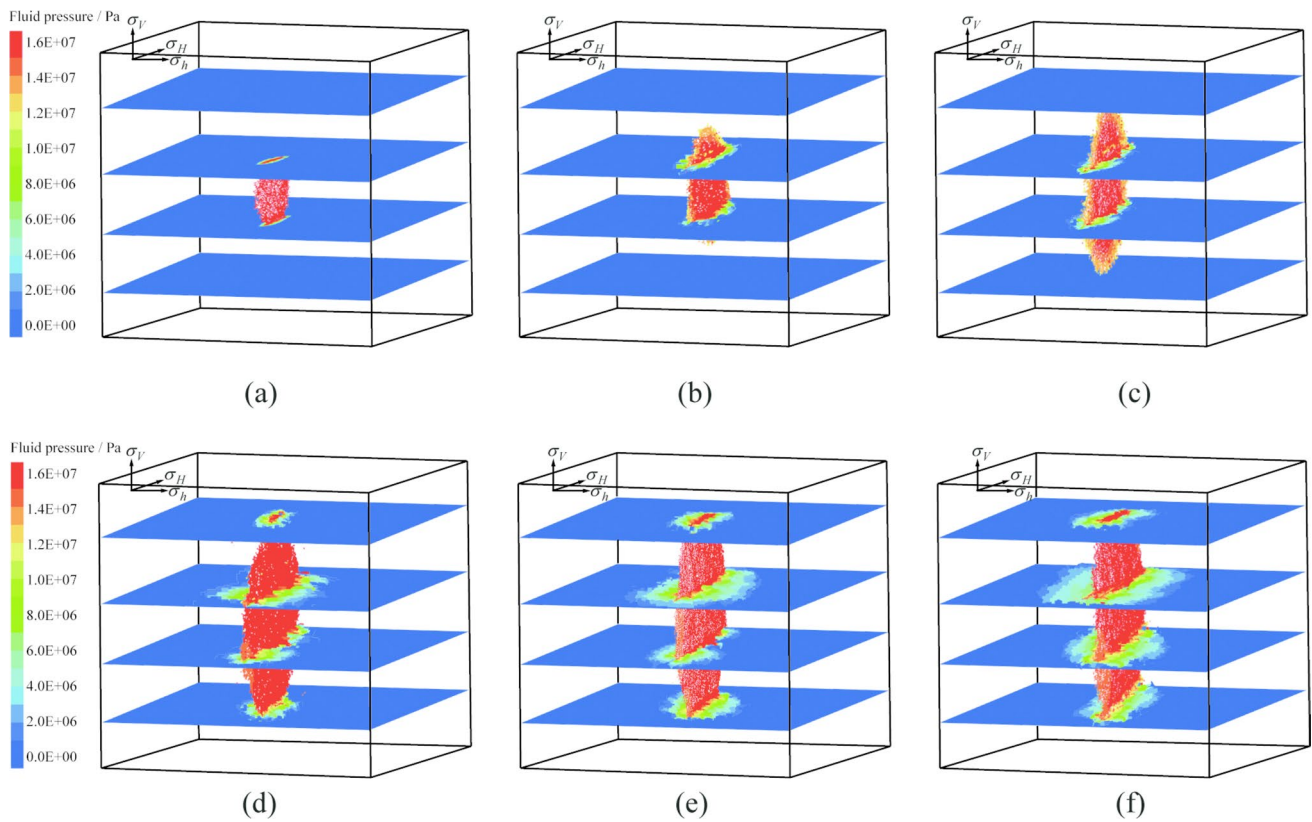


Fig. 13 HF extension pattern at different pumping moments for variable viscosity fracturing (firstly 0–5 s: 200 mPa s; secondly 5–10 s: 5 mPa s)

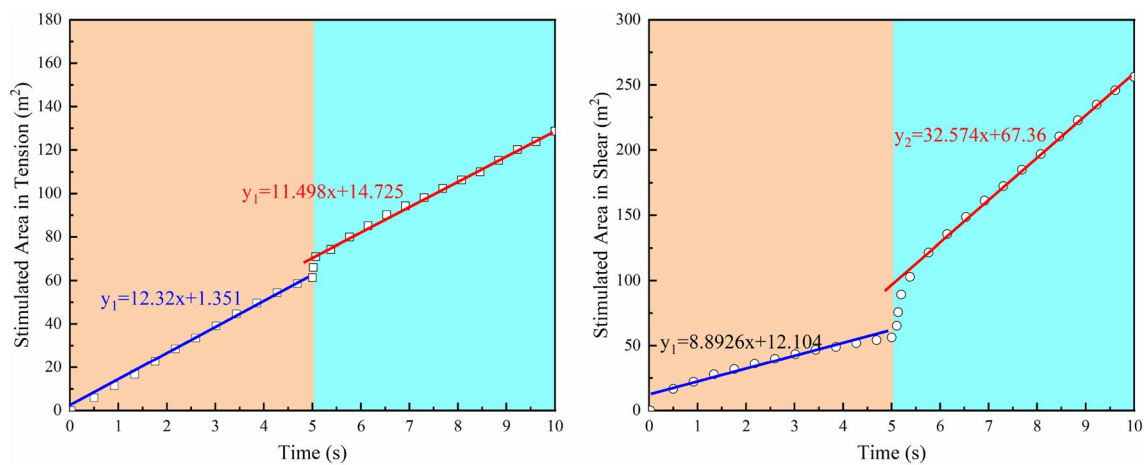


Fig. 14 Tension and shear fracture area changes during variable viscosity fracturing

area decreases to 11.49 m²/s, and that of the bedding fracture area increases to 32.57 m²/s. Therefore, alternating injection of high- and low-viscosity fracturing fluid can improve the balanced propagation of longitudinal and horizontal fractures, leading to effective 3D stimulation of reservoirs.

Experimental Studies

To verify the reliability of the numerical simulation results, a laboratory physical simulation experiment involving hydraulic fracturing was performed for Jurassic terrestrial shale from the Sichuan basin. The vertical

propagation pattern of HFs is analyzed with variations in the in situ stress difference, fracturing fluid viscosity, and injection rate via AE monitoring and 3D reconstruction of the fracture surface.

Experimental setup and sample preparation

The experiments were conducted using a triaxial hydraulic fracturing simulation system, as illustrated in Fig. 15. The system was capable of exerting a maximum axial force of 2000 kN and a maximum confining pressure of 140 MPa. The plunger pump used in the system had a maximum capacity of 260 mL and an injection rate of 0.001–100 mL/min. It could also generate a maximum output pressure of 65 MPa. During the experiments, eight acoustic emission sensors were utilized with a frequency range of 125–750 kHz. The specimen is $\phi 100 \text{ mm} \times 200 \text{ mm}$ and a blind hole (12.0 mm

in diameter and 113.5 mm in length) is drilled in its center as a simulated borehole.

Experimental parameters

In designing the laboratory-scale hydraulic fracturing experiments, scaling laws are followed to ensure that stable fracture propagation is representative of actual field conditions. A general scaling law for hydraulic fracturing was derived by de Pater et al. It requires that the sample has low fracture toughness and permeability. The fracturing fluid discharge rate in the field is 5–20 m^3/min , which is converted into 3–12 mL/min in the experiment. The confining pressure is 20 MPa, and the fracturing fluid viscosity is 3 and 40 mPa s. The experimental parameters are listed in Table 3.

The experimental proceeding is as follows: First, the rock sample is placed in the core chamber, and the confining pressure and vertical pressure are applied according

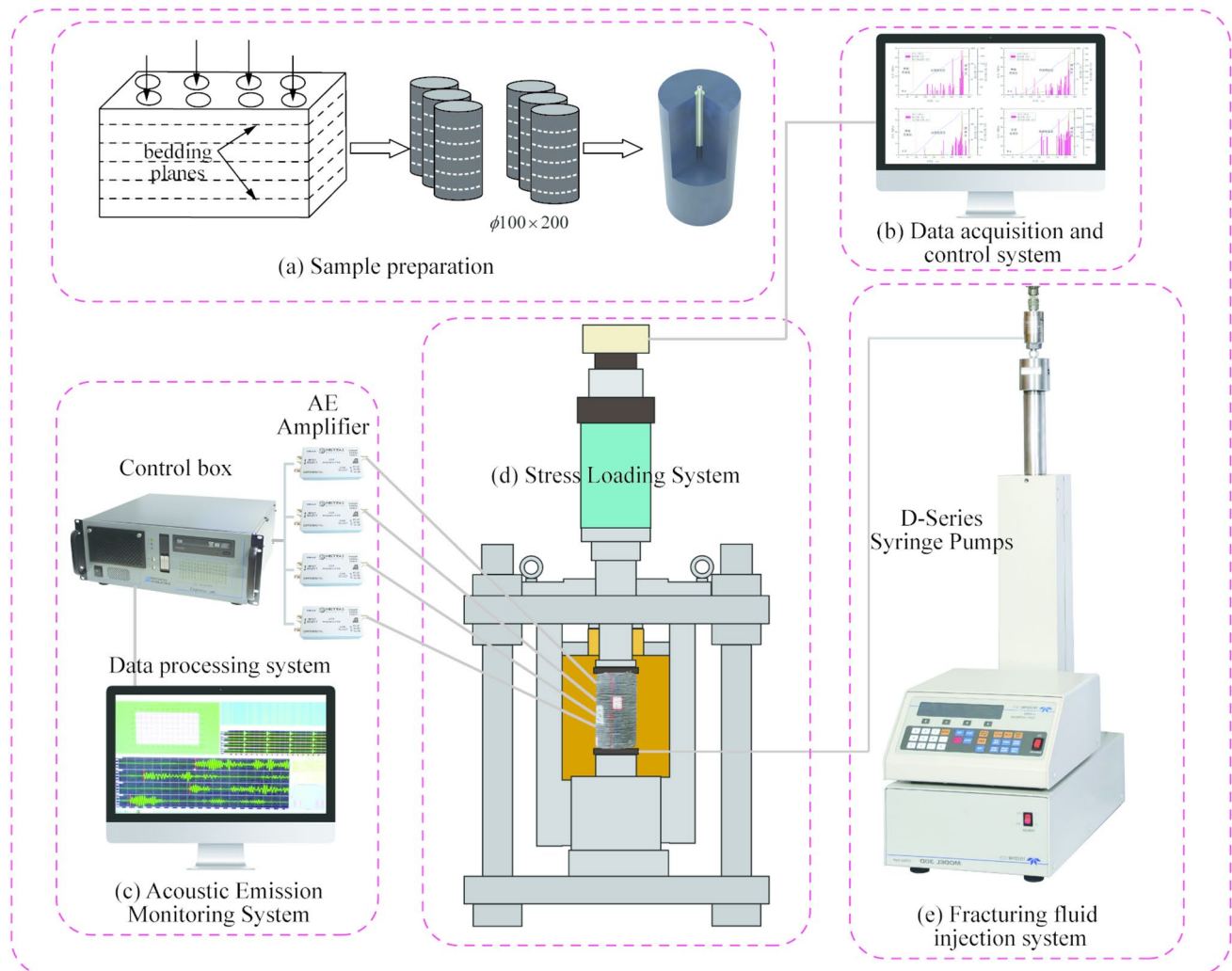


Fig. 15 Experimental apparatus and sample preparation

Table 3 Experimental parameters and evaluation results

Sample no	Confining stress (MPa)	Axial stress (MPa)	Injection rate (mL/min)	Fluid viscosity (mPa s)	Tension crack area (mm ²)	Shear crack area (mm ²)	Fracture volume density (mm ⁻¹)	Breakdown pressure (MPa)
F-1	20	24	3	3	4459	11,929	0.0104	41.94
F-2	20	32	3	3	13,307	7971	0.0135	42.65
F-3	20	24	6	3	12,152	5942	0.0114	35.01
F-4	20	24	12	3	6548	14,939	0.0136	35.93
F-5	20	24	3	40	10,015	8911	0.0121	43.65

to the parameters in Table 3. Second, turn on the plunger pump. The pressure changes at the wellhead are recorded. Simultaneously, the AE monitoring system is turned on to monitor the number of internal impacts and their locations during fracturing. The AE threshold value is 45 dB. The sampling frequency is 1 MHz, and the preamplifier gain is set as 40 dB. When the wellhead pressure drops sharply, the pump is turned off, and the data acquisition system is shut down. Finally, the fracture morphology of the sample after fracturing is scanned using a high-precision 3D scanner. The 3D fracture surfaces of the sample are reconstructed using Geomagic, and the spatial complexity of the fractures is measured using the fracture volume density. The HF extension pattern and pumping pressure curve are shown in Fig. 16.

Experimental results

Effects of vertical in situ stress difference

The in situ stress is the main factor controlling the extent of the HF network. In this test, two different vertical stress difference coefficients are used. When the coefficient is 0.25 (F-1), it is easier to activate weak planes because the normal stress acting on the bedding plane is lower. In cases where hydraulic fractures extend vertically to weaker bedding planes, the fracturing fluid has the potential to be lost through these planes, ultimately leading to the termination of the fractures. Hence, the fractures travel for shorter distances in the longitudinal direction. When the vertical stress difference coefficient increases to 0.6 (F-2), a noticeable longitudinal fracture is formed inside the sample with an area of 13,307 mm², which is 1.98 times larger than that of sample F-1.

Effects of fracturing fluid injection rate

The vertical propagation of fractures is observed when the injection rates are 3 mL/min (F-1), 6 mL/min (F-3), and 12 mL/min (F-4) under an axial stress of 24 MPa. When the fracturing fluid discharge rate is 3 mL/min, after HFs propagate and encounter bedding planes, their longitudinal

propagation is inhibited by the planes. The fractures are terminated between the two bedding planes, and the fracture volume density is 0.0104 mm⁻¹. At a fracturing fluid discharge rate of 6 mL/min, HFs cross the two bedding planes longitudinally and extend to the upper surface of the specimen. The fracture volume density equals 0.0114 mm⁻¹. When the fracturing fluid discharge rate continues to increase to 12 mL/min, a longitudinal penetrating fracture is formed inside the sample, and three bedding planes are activated simultaneously. The fracture volume density is 0.0136 mm⁻¹. In summary, as the discharge rate increases, the ability of HFs to cross the bedding planes improves, and larger fracture heights and ESRA can be obtained.

Effect of fracturing fluid viscosity

For a fracturing fluid viscosity of 3 mPa s (F-1), the HFs stop when they reach the adjacent bedding planes and cannot pass through the planes. Massive fracturing fluid is lost along the bedding planes, and the activated horizontal bedding fracture area is 11,929 mm². When the fracturing fluid viscosity increases to 40 mPa s (F-5), the vertical penetration ability of the fractures is enhanced, and they traverse several bedding planes in succession. However, because of the higher viscosity, the fracturing fluid filter loss distance along the bedding planes is reduced, and the activated horizontal bedding fracture area is only 8910 mm². The use of high-viscosity fracturing fluid results in a 25% increase in longitudinal penetration ability compared to low-viscosity fracturing fluid, according to the findings. This suggests that increasing the viscosity of the fracturing fluid is an effective way to enhance fracture penetration ability.

Pump pressure curves and AE responses

The pump pressure curve is useful for studying the HF propagation path pattern and predicting fracture penetration. The pump pressure curve for laminated shale reservoirs is divided into three main stages: the wellbore filling stage, the wellbore shut-in stage, and the post-peak stage. For sample F-1, at 0–80 s, fracturing fluid continuously

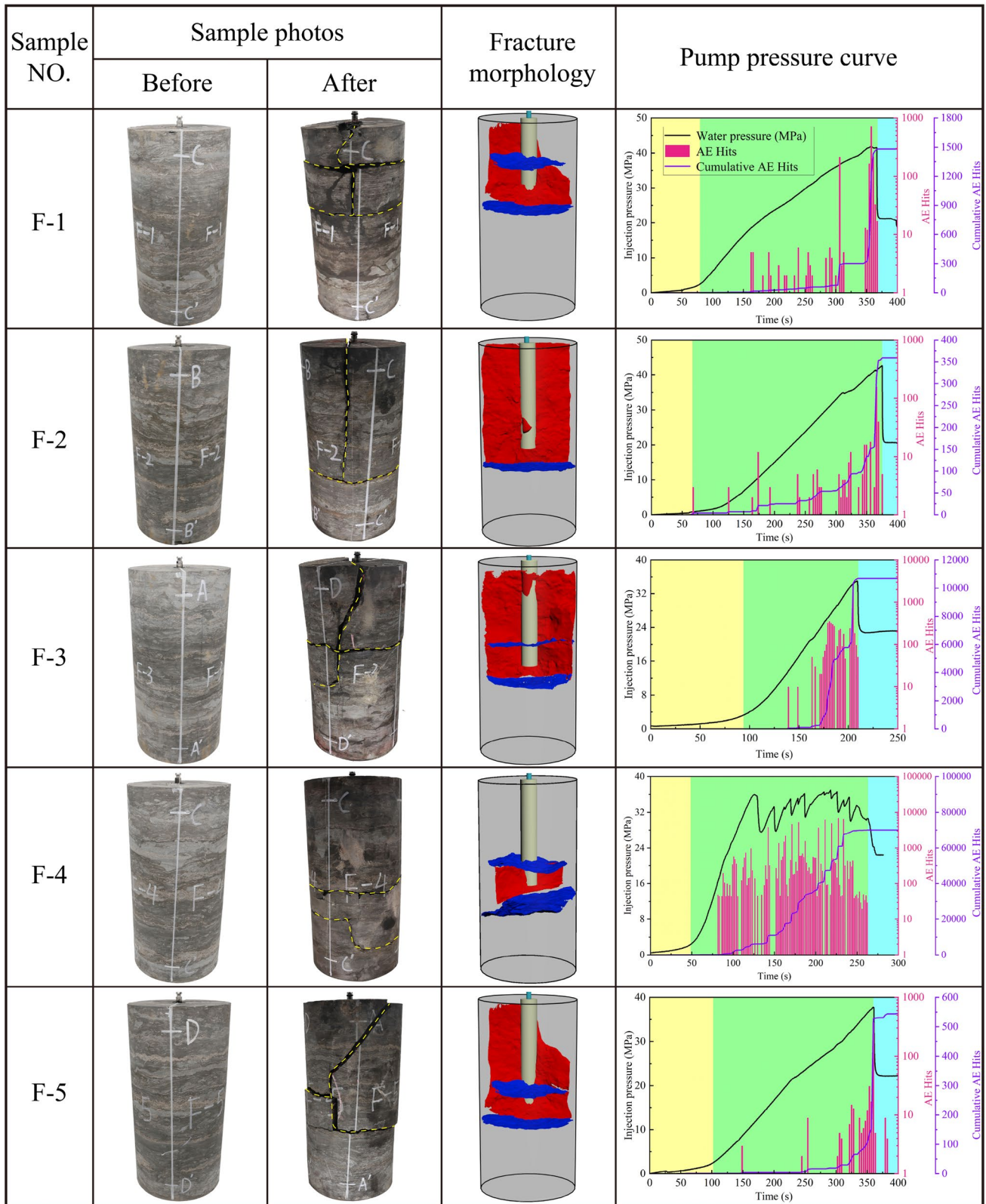


Fig. 16 HF expansion morphologies and pumping pressure curves

fills the microfractures connected to the wellbore. As the fluid injection time increases, various fractures inside the sample develop, propagate, and penetrate rapidly, and macroscopic main fractures start to appear and develop rapidly. The peak rupture pressure (41.94 MPa) is reached at approximately 370 s. The accumulated elastic energy inside the sample exceeds the limit, and the AE impact number peaks; thus, the rock sample ruptures. The cumulative AE impact number of sample F-2 is significantly reduced compared with that of sample F-1. The cumulative AE impact number increases continuously as the fracturing fluid discharge rate increases. This indicates an increase in the HF complexity. In particular, when the fracturing fluid discharge rate reaches 12 mL/min, the post-peak pump pressure curve fluctuates significantly, and the AE responses are abnormally active, suggesting continuous opening of new microfractures. When the fracturing fluid viscosity increases to 40 mPa s, it is more difficult for the fracturing fluid to enter the microfractures connected to the wellbore. Compared with sample F-1, the AE responses appear later and are mainly concentrated near the peak.

Field application

A proposed technology called inverse mixed volume fracturing process, which involves using high-viscosity glue fluid forward and high-displacement fast press holding, maybe a solution to the challenge of developing complex fracture networks in Jurassic terrestrial shale oil reservoirs that are stratigraphically developed and not conducive to fracture height expansion. Different from the conventional pumping process, this process first pumps high-viscosity fracturing fluid into the formation to form the main fracture that breaks through the laminar interference and then injects low-viscosity fracturing fluid to activate the laminar interaction with the main fracture, thus increasing the fracture complexity and maximizing the shale stimulated reservoir volume.

Currently, this technology has been applied on five horizontal wells in the Fuxing area (Fig. 17). Among them, the volume of front fluid is more than 150m³, viscosity is more than 50 mPa s, and displacement is larger than 15m³/min. Micro-seismic monitoring showed that the fracture fluctuation height was 50 m, the fracture bandwidth was 85 m, the stimulated volume of single-section was 45 × 10⁴m³, and

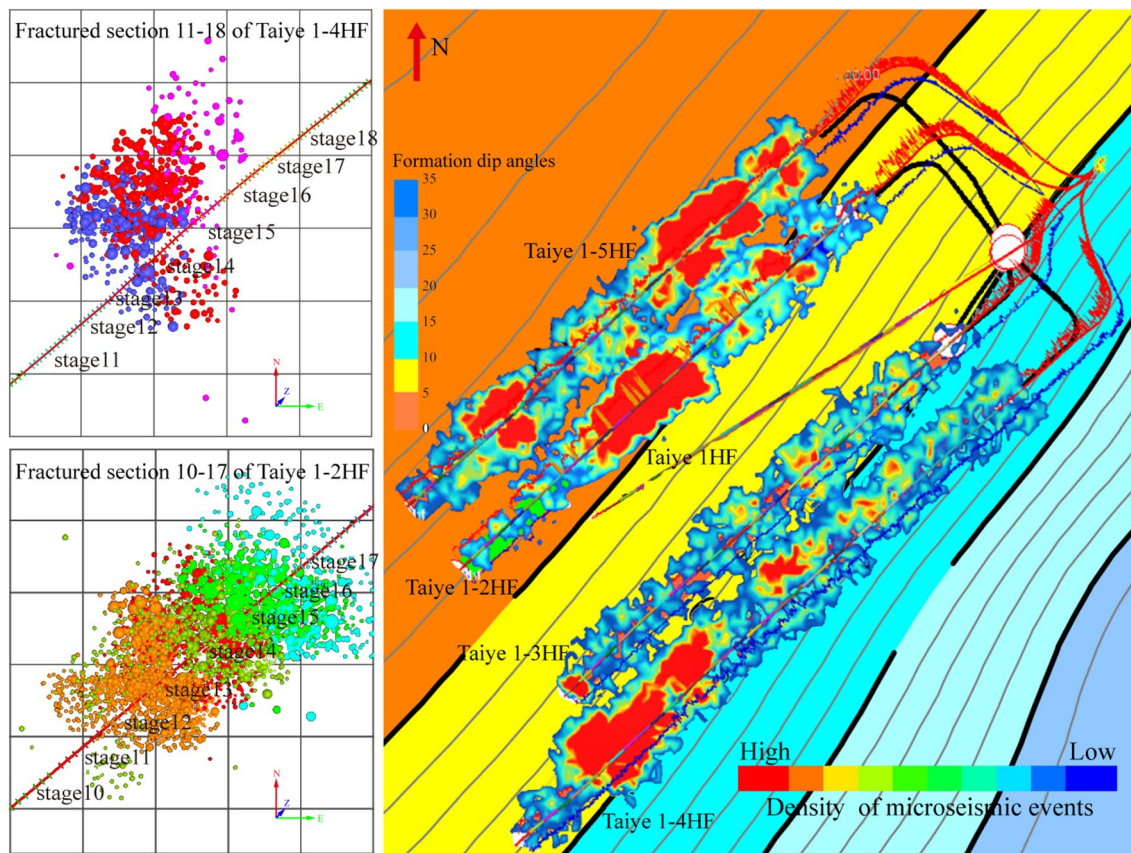


Fig. 17 Cloud map of the micro-seismic event density distribution of TY-1 well group

the volume of full well stimulation was $1600 \times 10^4 \text{ m}^3$. The maximum daily gas production and daily oil production were $6 \times 10^4 \text{ m}^3$ and 45t, respectively.

Conclusions

This study utilized a three-dimensional discrete lattice algorithm to investigate the longitudinal through-layer propagation pattern of hydraulic fractures in stratified shale oil reservoirs. The findings of this research are as follows:

- (1) The adhesive strength of the bedding plane significantly influences the hydraulic fracture propagation pattern. Increasing the friction coefficient of the laminated surface from 0.15 to 0.91 resulted in a twofold increase in fracture height.
- (2) Hydraulic cracks are more likely to directly cross the bedding plane as the difference between the vertical stress and the minimum horizontal principal stress rises. However, this may lead to a significant decrease in the opening area of the bedding plane due to the increase in normal stress acting on it.
- (3) Increasing the fluid viscosity and injection rate can facilitate the hydraulic fracture crossing the bedding planes.
- (4) Implementing reverse-sequence fracturing technology in stratified shale oil reservoirs can generate fishbone-like fractures, thereby dramatically enhancing hydraulic fracture complexity and stimulating reservoir volume.

Funding This study was financially supported by the National Natural Science Foundation of China (No. 52104046, No. 52174017).

Declarations

Conflict of interest The authors declare that they have no known competing financial interests or personal relationships that could have appeared to influence the work reported in this paper.

Open Access This article is licensed under a Creative Commons Attribution 4.0 International License, which permits use, sharing, adaptation, distribution and reproduction in any medium or format, as long as you give appropriate credit to the original author(s) and the source, provide a link to the Creative Commons licence, and indicate if changes were made. The images or other third party material in this article are included in the article's Creative Commons licence, unless indicated otherwise in a credit line to the material. If material is not included in the article's Creative Commons licence and your intended use is not permitted by statutory regulation or exceeds the permitted use, you will need to obtain permission directly from the copyright holder. To view a copy of this licence, visit <http://creativecommons.org/licenses/by/4.0/>.

References

- Al-Fatlawi O, Hossain M, Essa A (2019) Optimization of Fracture Parameters for Hydraulic Fractured Horizontal Well in a Heterogeneous Tight Reservoir: An Equivalent Homogeneous Modelling Approach. SPE Kuwait Oil Gas Show Conf. D023S004R008
- Alipour M, Esatyana E, Sakhaee-Pour A et al (2021) Characterizing fracture toughness using machine learning. J Pet Sci Eng 200:108202. <https://doi.org/10.1016/j.petrol.2020.108202>
- Altawati F, Emadi H, Khalil R (2021) An experimental study to investigate the physical and dynamic elastic properties of eagle ford shale rock samples. J Pet Explor Prod Technol 11:3389–3408. <https://doi.org/10.1007/s13202-021-01243-w>
- Bakhshi E, Golsanami N, Chen L (2021) Numerical modeling and lattice method for characterizing hydraulic fracture propagation: a review of the numerical, experimental, and field studies. Arch Comput Methods Eng 28:3329–3360. <https://doi.org/10.1007/s11831-020-09501-6>
- Belyadi H, Fathi E, Belyadi F (2016) Hydraulic Fracturing in Unconventional Reservoirs: Theories, Operations, and Economic Analysis. Gulf Professional Publishing.
- Beugelsdijk LJJ, de Pater CJ, Sato K (2000) Experimental Hydraulic Fracture Propagation in a Multi-Fractured Medium. SPE Asia Pacific Conf. Integr. Model. Asset Manag. SPE-59419-MS
- Chang X, Wang G, Liang Z et al (2017) Study on grout cracking and interface debonding of rockbolt grouted system. Constr Build Mater 135:665–673. <https://doi.org/10.1016/j.conbuildmat.2017.01.031>
- Chang X, Xu E, Guo Y et al (2022) Experimental study of hydraulic fracture initiation and propagation in deep shale with different injection methods. J Pet Sci Eng 216:110834. <https://doi.org/10.1016/j.petrol.2022.110834>
- Damjanac B, Cundall P (2016) Application of distinct element methods to simulation of hydraulic fracturing in naturally fractured reservoirs. Comput Geotech 71:283–294. <https://doi.org/10.1016/j.compgeo.2015.06.007>
- Damjanac B, Cundall P (2016b) Application of distinct element methods to simulation of hydraulic fracturing in naturally fractured reservoirs. Comput Geotech 71:283–294. <https://doi.org/10.1016/J.COMPGEO.2015.06.007>
- Deng H, Sheng G, Zhao H et al (2022) Integrated optimization of fracture parameters for subdivision cutting fractured horizontal wells in shale oil reservoirs. J Pet Sci Eng 212:110205. <https://doi.org/10.1016/j.petrol.2022.110205>
- Dheyauldeen A, Alkhafaji H, Alfarge D et al (2022) Performance evaluation of analytical methods in linear flow data for hydraulically-fractured gas wells. J Pet Sci Eng 208:109467. <https://doi.org/10.1016/j.petrol.2021.109467>
- Esatyana E, Sakhaee-Pour A, Sadooni FN, Al-Kuwari HA-S (2020) Nanoindentation of shale cuttings and its application to core measurements. Petrophys SPWLA J Form Eval Reserv Descr 61:404–416
- Esatyana E, Alipour M, Sakhaee-Pour A (2021) Characterizing anisotropic fracture toughness of shale using nanoindentation. SPE Reserv Eval Eng 24:590–602. <https://doi.org/10.2118/205488-PA>
- Gu H, Weng X, Lund J et al (2012) Hydraulic fracture crossing natural fracture at nonorthogonal angles: a criterion and its validation. SPE Prod Oper 27:20–26. <https://doi.org/10.2118/139984-PA>
- Gu H, Siebrits E, Sabourov A (2008) Hydraulic-Fracture Modeling With Bedding Plane Interfacial Slip SPE East Reg East Sect Jt Meet SPE-117445-MS
- Guo P, Li X, Li S et al (2021) Quantitative analysis of anisotropy effect on hydrofracturing efficiency and process in shale using X-ray

- computed tomography and acoustic emission. *Rock Mech Rock Eng* 54:5715–5730. <https://doi.org/10.1007/s00603-021-02589-7>
- Heng S, Li X, Liu X, Chen Y (2020) Experimental study on the mechanical properties of bedding planes in shale. *J Nat Gas Sci Eng* 76:103161. <https://doi.org/10.1016/J.JNGSE.2020.103161>
- Huang L, Dontsov E, Fu H et al (2022) Hydraulic fracture height growth in layered rocks: perspective from DEM simulation of different propagation regimes. *Int J Solids Struct* 238:111395. <https://doi.org/10.1016/j.ijsolstr.2021.111395>
- Li W, Sakhaee-Pour A (2016) Macroscale young's moduli of shale based on nanoindentations. *Petrophysics - SPWLA J Form Eval Reserv Descr* 57:597–603
- Li Q, Xing H, Liu J, Liu X (2015) A review on hydraulic fracturing of unconventional reservoir. *Petroleum* 1:8–15. <https://doi.org/10.1016/j.petlm.2015.03.008>
- Li N, Zhang S, Zou Y et al (2018) Acoustic emission response of laboratory hydraulic fracturing in layered shale. *Rock Mech Rock Eng* 51:3395–3406. <https://doi.org/10.1007/s00603-018-1547-5>
- Li M, Zhou F, Sun Z et al (2022) Experimental study on plugging performance and diverted fracture geometry during different temporary plugging and diverting fracturing in Jimusar shale. *J Pet Sci Eng* 215:110580. <https://doi.org/10.1016/j.petrol.2022.110580>
- Liu Q, Liang B, Sun W et al (2022) Experimental study on hydraulic fracturing of bedding shale considering anisotropy effects. *ACS Omega* 7:22698–22713
- Muther T, Qureshi HA, Syed FI et al (2022) Unconventional hydrocarbon resources: geological statistics, petrophysical characterization, and field development strategies. *J Pet Explor Prod Technol* 12:1463–1488. <https://doi.org/10.1007/s13202-021-01404-x>
- Peirce A, Detournay E (2008) An implicit level set method for modeling hydraulically driven fractures. *Comput Methods Appl Mech Eng* 197:2858–2885. <https://doi.org/10.1016/j.cma.2008.01.013>
- Pierce M, Cundall P, Potyondy D, Ivars DM (2007) A Synthetic Rock Mass Model For Jointed Rock. 1st Canada-U.S. Rock Mech. Symp. ARMA-07–042
- Potyondy DO (2015) The bonded-particle model as a tool for rock mechanics research and application: current trends and future directions. *Geosystem Eng* 18:1–28. <https://doi.org/10.1080/12269328.2014.998346>
- Potyondy DO, Cundall PA (2004) A bonded-particle model for rock. *Int J Rock Mech Min Sci* 41:1329–1364. <https://doi.org/10.1016/j.ijrmms.2004.09.011>
- Qin M, Yang D (2023) Numerical investigation of hydraulic fracture height growth in layered rock based on aerodynamics. *Theor Appl Fract Mech* 125:103885. <https://doi.org/10.1016/j.tafmec.2023.103885>
- Rueda Cordero JA, Mejia Sanchez EC, Roehl D, Pereira LC (2019) Hydro-mechanical modeling of hydraulic fracture propagation and its interactions with frictional natural fractures. *Comput Geotech* 111:290–300. <https://doi.org/10.1016/j.compgeo.2019.03.020>
- Sakhaee-Pour A, Li W (2018) Two-scale geomechanics of shale. *SPE Reserv Eval Eng* 22:161–172. <https://doi.org/10.2118/189965-PA>
- Savitski AA, Detournay E (2002) Propagation of a penny-shaped fluid-driven fracture in an impermeable rock: asymptotic solutions. *Int J Solids Struct* 39:6311–6337. [https://doi.org/10.1016/S0020-7683\(02\)00492-4](https://doi.org/10.1016/S0020-7683(02)00492-4)
- Soltanmohammadi R, Irajli S, De Almeida TR, et al (2021) Insights into Multi-Phase Flow Pattern Characteristics and Petrophysical Properties in Heterogeneous Porous Media. In: Second EAGE Conference on Pre-Salt Reservoir. European Association of Geoscientists & Engineers, pp 1–5
- Tan P, Pang H, Zhang R et al (2020) Experimental investigation into hydraulic fracture geometry and proppant migration characteristics for southeastern Sichuan deep shale reservoirs. *J Pet Sci Eng* 184:106517. <https://doi.org/10.1016/J.PETROL.2019.106517>
- Tan P, Jin Y, Pang H (2021) Hydraulic fracture vertical propagation behavior in transversely isotropic layered shale formation with transition zone using XFEM-based CZM method. *Eng Fract Mech* 248:107707. <https://doi.org/10.1016/j.engfracmech.2021.107707>
- Tang H, Wang S, Zhang R et al (2019) Analysis of stress interference among multiple hydraulic fractures using a fully three-dimensional displacement discontinuity method. *J Pet Sci Eng* 179:378–393. <https://doi.org/10.1016/J.PETROL.2019.04.050>
- Wang H, Liu H, Wu HA, Wang XX (2015) A 3D numerical model for studying the effect of interface shear failure on hydraulic fracture height containment. *J Pet Sci Eng* 133:280–284. <https://doi.org/10.1016/j.petrol.2015.06.016>
- Wang Y, Li X, Zhao B, Zhang Z (2020) Numerical simulation of particle plugging in hydraulic fracture by element partition method. *Int J Numer Anal Methods Geomech* 44:1857–1879. <https://doi.org/10.1002/nag.3109>
- Wang Y, Hou B, Wang D, Jia Z (2021) Features of fracture height propagation in cross-layer fracturing of shale oil reservoirs. *Pet Explor Dev* 48:469–479. [https://doi.org/10.1016/S1876-3804\(21\)60038-1](https://doi.org/10.1016/S1876-3804(21)60038-1)
- Warpinski NR, Teufel LW (1987) Influence of geologic discontinuities on hydraulic fracture propagation (includes associated papers 17011 and 17074). *J Pet Technol* 39:209–220. <https://doi.org/10.2118/13224-PA>
- Wu S, Gao K, Feng Y, Huang X (2022) Influence of slip and permeability of bedding interface on hydraulic fracturing: A numerical study using combined finite-discrete element method. *Comput Geotech* 148:104801. <https://doi.org/10.1016/j.compgeo.2022.104801>
- Wu R, Bungler AP, Jeffrey RG, Siebrits E (2008) A comparison of numerical and experimental results of hydraulic fracture growth into a zone of lower confining stress. In: The 42nd US Rock Mechanics Symposium (USRMS). OnePetro
- Xie J, Tang J, Yong R et al (2020) A 3-D hydraulic fracture propagation model applied for shale gas reservoirs with multiple bedding planes. *Eng Fract Mech* 228:106872. <https://doi.org/10.1016/j.engfracmech.2020.106872>
- Yushi Z, Xinfang M, Shicheng Z et al (2016) Numerical investigation into the influence of bedding plane on hydraulic fracture network propagation in shale formations. *Rock Mech Rock Eng* 49:3597–3614. <https://doi.org/10.1007/s00603-016-1001-5>
- Yushi Z, Xinfang M, Tong Z et al (2017) Hydraulic fracture growth in a layered formation based on fracturing experiments and discrete element modeling. *Rock Mech Rock Eng* 50:2381–2395. <https://doi.org/10.1007/s00603-017-1241-z>
- Zeng Q-D, Yao J, Shao J (2018) Numerical study of hydraulic fracture propagation accounting for rock anisotropy. *J Pet Sci Eng* 160:422–432. <https://doi.org/10.1016/j.petrol.2017.10.037>
- Zeng Q, Bo L, Li Q et al (2023) Numerical investigation of hydraulic fracture propagation interacting with bedding planes. *Eng Fract Mech* 291:109575. <https://doi.org/10.1016/j.engfracmech.2023.109575>
- Zhang C, Song Z, Zhao Y (2023) Staged multicluster hydraulic fracture propagation mechanism and its influencing factors in horizontal wells for CBM development. *Energy Sci Eng* 11:448–462. <https://doi.org/10.1002/ese3.1315>
- Zhang J, Yu Q, Li Y et al (2023b) Hydraulic fracture vertical propagation mechanism in interlayered brittle shale formations: an experimental investigation. *Rock Mech Rock Eng* 56:199–220. <https://doi.org/10.1007/s00603-022-03094-1>
- Zhao Q, Lisjak A, Mahabadi O et al (2014) Numerical simulation of hydraulic fracturing and associated microseismicity using finite-discrete element method. *J Rock Mech Geotech Eng* 6:574–581. <https://doi.org/10.1016/j.jrmge.2014.10.003>
- Zhao K, Stead D, Kang H et al (2020) Investigating the interaction of hydraulic fracture with pre-existing joints based on lattice spring modeling. *Comput Geotech* 122:103534. <https://doi.org/10.1016/j.compgeo.2020.103534>

Zhou W, Shi G, Wang J et al (2022) The influence of bedding planes on tensile fracture propagation in shale and tight sandstone. *Rock Mech Rock Eng.* <https://doi.org/10.1007/s00603-021-02742-2>

Publisher's Note Springer Nature remains neutral with regard to jurisdictional claims in published maps and institutional affiliations.